CHEMICAL PHYSICS

Distinct armchair and zigzag charge transport through single polycyclic aromatics

Miao Zhang[1,2,3]†, Zewen Wu[4]†, Hongxing Jia[5]†, Peihui Li[1]†, Lei Yang[3], Jie Hao[1], Jinying Wang[1,6], Enyu Zhang[1], Linan Meng[2], Zhuang Yan[2], Yi Liu[3], Pingwu Du[5]*, Xianghua Kong[4]*, Shengxiong Xiao[3]*, Chuancheng Jia[1,2]*, Xuefeng Guo[1,2]*

In aromatic systems with large π-conjugated structures, armchair and zigzag configurations can affect each material's electronic properties, determining their performance and generating certain quantum effects. Here, we explore the intrinsic effect of armchair and zigzag pathways on charge transport through single hexabenzocoronene molecules. Theoretical calculations and systematic experimental results from static carbon-based single-molecule junctions and dynamic scanning tunneling microscope break junctions show that charge carriers are preferentially transported along the hexabenzocoronene armchair pathway, and thus, the corresponding current through this pathway is approximately one order of magnitude higher than that through the zigzag pathway. In addition, the molecule with the zigzag pathway has a smaller energy gap. In combination with its lower off-state conductance, it shows a better field-effect performance because of its higher on-off ratio in electrical measurements. This study on charge transport pathways offers a useful perspective for understanding the electronic properties of π-conjugated systems and realizing high-performance molecular nanocircuits toward practical applications.

INTRODUCTION

In carbon nanomaterials, in which aromatic rings are the basic structural unit, the unit configuration can affect the electronic structures and physical properties of these materials. For example, the armchair and zigzag edges of graphene nanoribbons have a major impact on the stability, magnetism, and energy band structure of the materials (*1*, *2*). In narrow armchair-edged graphene nanoribbon with certain structural periods, quantum confinement is expected to open substantial electronic bandgaps, thus giving the material semiconducting properties. In contrast, a zigzag graphene nanoribbon of a similar width will maintain its semimetallic properties with almost a negligible bandgap. Furthermore, the zigzag edges of graphene host spin-polarized electronic edge states, which can be used in spintronics. In addition, both the zigzag and armchair configurations also have notable effects on the energy band structures of carbon nanotubes (CNTs). CNTs with zigzag transport exhibit metallic properties, while those with armchair transport have semiconducting properties. Further control of charge transport between the zigzag and armchair directions of chiral CNTs could cause them to have rich energy band structures. To enable better understanding and utilization of carbon nanomaterials, it is critically important to reveal the influence of armchair and zigzag configurations on charge transport from the perspective of the single-molecule level.

Single-molecule junction techniques, including both dynamic and static junctions, provide effective tools for characterization of the charge transport properties of molecules at the single-molecule level, thus uncovering the inherent physical properties and quantum effects of these molecules (*3*–*5*). Specifically, on the basis of the different conductivity properties of single molecules, the constructive and destructive quantum interference effects that occur during the charge transport process through the different molecular orbital energy levels have been studied widely (*6*–*9*). In addition, the phenomenon of increased conductance caused by the superposition of multiple conductive channels has also been deeply studied through single-molecule junction techniques (*10*, *11*).

Polycyclic aromatic hydrocarbons with graphene-like structures are generally regarded as the basic building blocks for functional carbon materials (*12*–*14*). Hexabenzocoronene (HBC) is a typical fused-ring aromatic molecule that has a perfect discoidal structure. Because of their unique structural and electronic properties, HBC molecules have great potential for use in the fields of electronics and optoelectronics (*15*–*20*). In addition, the close arrangement of their benzene rings allows simultaneous distribution of both armchair and zigzag structures in HBC molecules. Here, we investigate the charge transport through the armchair and zigzag transport pathways of single HBC molecules using both dynamic scanning tunneling microscope break junctions (STM-BJs) and static graphene-molecule-graphene single-molecule junctions (GMG-SMJs). The effects of these different transport pathways on

---

[1]Center of Single-Molecule Sciences, Institute of Modern Optics, Frontiers Science Center for New Organic Matter, College of Electronic Information and Optical Engineering, Nankai University, 38 Tongyan Road, Jinnan District, Tianjin 300350, China. [2]Beijing National Laboratory for Molecular Sciences, National Biomedical Imaging Center, College of Chemistry and Molecular Engineering, Peking University, 292 Chengfu Road, Haidian District, Beijing 100871, China. [3]The Education Ministry Key Lab of Resource Chemistry, Joint International Research Laboratory of Resource Chemistry, Ministry of Education, Shanghai Key Laboratory of Rare Earth Functional Materials, Shanghai Frontiers Science Center of Biomimetic Catalysis, College of Chemistry and Materials Science, Shanghai Normal University, Shanghai 200234, China. [4]College of Physics and Optoelectronic Engineering, Shenzhen University, Shenzhen 518060, China. [5]Hefei National Research Center for Physical Sciences at the Microscale, Anhui Laboratory of Advanced Photon Science and Technology, CAS Key Laboratory of Materials for Energy Conversion, Department of Materials Science and Engineering, iChEM, University of Science and Technology of China, 96 Jinzhai Road, Hefei, Anhui Province 230026, China. [6]Network for Computational Nanotechnology, College of Engineering, Purdue University, 298 Nimitz Dr., West Lafayette, IN 47906, USA.
*Corresponding author. Email: guoxf@pku.edu.cn (X.G.); jiacc@nankai.edu.cn (C.J.); xiaosx@shnu.edu.cn (S.X.); kongxianghuaphysics@szu.edu.cn (X.K); dupingwu@ustc.edu.cn (P.D.)

†These authors contributed equally to this work.

the performances of single-molecule field-effect transistors are also explored.

RESULTS AND DISCUSSION

Design of HBC molecules

Two HBC molecules were designed with different central structures and external sites to enable construction of armchair and zigzag channels. The synthesis details are provided in the Supplementary Materials (section S1 and figs. S1 to S15). These two channels pass through the molecular center to ensure that they are the dominant channels in each molecule. In the armchair channel HBC molecule (*ac*-HBC), the charge is expected to be transported along the armchair-dominated conductive channel (Fig. 1A), while the charge in the zigzag channel HBC molecule (*zc*-HBC) will be transported along the zigzag-dominated conductive channel (Fig. 1C). To increase the solubility of *ac*-HBC and *zc*-HBC molecules, R^1/R^2 groups (where R^1 is 1,3,5-trimethylbenzene and R^2 is dodecyloxy) are hung around the center of the target molecules to ensure that these molecules can be connected successfully with the electrodes in the subsequent solution assembly process (*17*). The density-of-state distributions of the highest occupied molecular orbitals (HOMOs) of *ac*-HBC and *zc*-HBC molecules, which are expected to dominate charge transport, are simulated theoretically. Obvious densities of states can be observed along the main transport channels in both molecules (Fig. 1, B and D), providing a basis for directional charge transport. Although there are other small density-of-state distributions in the molecular framework, their contribution to charge transport is negligible because of the ultralow transmission probability at their corresponding positions.

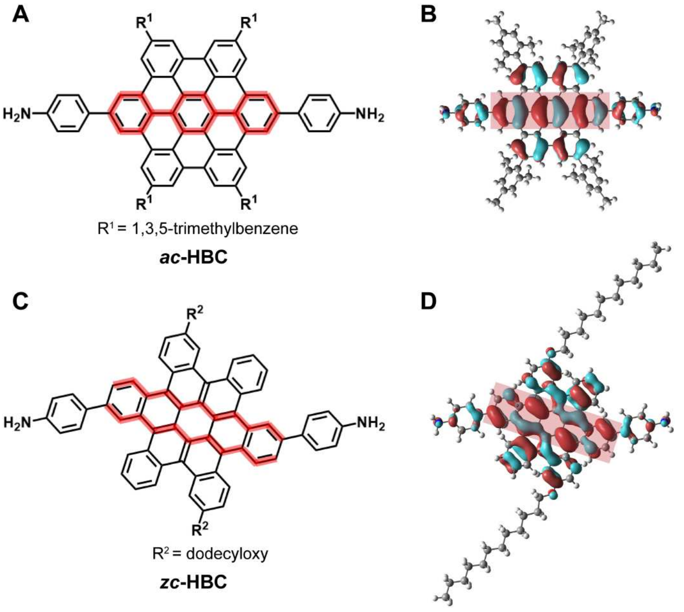

Fig. 1. Molecular designs of *ac*-HBC and *zc*-HBC. (**A** and **C**) Molecular structures of *ac*-HBC and *zc*-HBC, respectively. (**B** and **D**) Density-of-state distributions for the HOMOs of *ac*-HBC and *zc*-HBC, respectively. The isosurface value for both spatial charge density distributions is ~0.015 eÅ^{-3}. Red highlights indicate the main conduction channels for these molecules.

The structural characteristics described above form the basis for both armchair and zigzag charge transport through the molecules.

Conductance of armchair and zigzag channels

To study the charge transport behavior of armchair and zigzag channels, dynamic Au-(*ac*-HBC)-Au and Au-(*zc*-HBC)-Au single-molecule junctions (Fig. 2, A and D) were constructed using the STM-BJ technique, which can measure the conductance of *ac*-HBC and *zc*-HBC molecules statistically. Specifically, single-molecule junctions were formed and broken in 1,2,4-trichlorobenzene (TCB) solutions containing *ac*-HBC and *zc*-HBC molecules, respectively. Repeated measurements of the conductance as a function of the tip-to-substrate displacement were performed to generate conductance versus displacement curves. Two-dimensional (2D) conductance-displacement histograms of *ac*-HBC and *zc*-HBC molecules under 0.1 V of bias are shown in Fig. 2 (B and E), respectively. Typical single traces of the junctions can be seen in fig. S16. The gray traces and fig. S17 illustrate the tunneling decay that occurs following breakage of the gold atomic contacts in the pure solvent, while a conductance plateau corresponding to the molecular conductance can be found in the solution containing the target molecules. The conductivity characteristics at integer multiples of G_0 (where $G_0 = 2e^2/h$) can be observed, along with characteristics below G_0 at specific molecular values. Specific conductance peaks for the target molecules can be determined from these 2D conductance-displacement histograms and 1D conductance histograms (Fig. 2, B and E, and their corresponding insets, respectively). The conductance peak for the *zc*-HBC molecule at ~1.8×10^{-6} G_0 (≈0.14 nS) can be observed, while the conductance peak for the

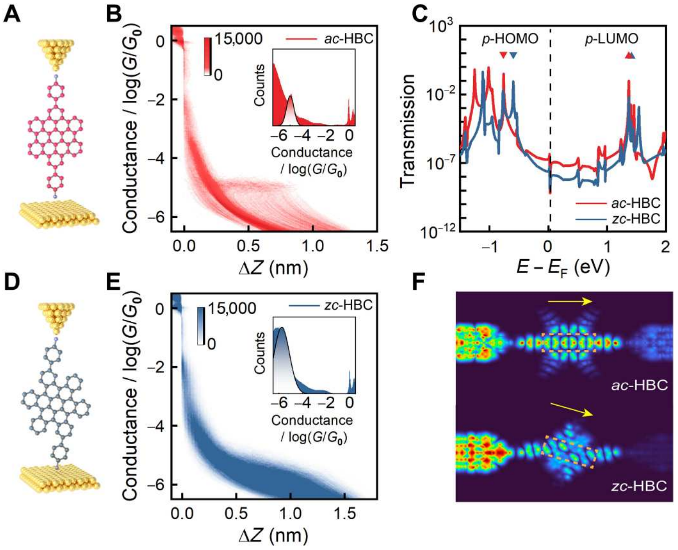

Fig. 2. Charge transport of dynamic single-molecule junctions. (**A** and **D**) Schematics of the Au-(*ac*-HBC)-Au single-molecule junction and the Au-(*zc*-HBC)-Au single-molecule junction, respectively. (**B** and **E**) 2D conductance-displacement histograms with 1D conductance histograms (insets) for *ac*-HBC and *zc*-HBC junctions, respectively. The conductance values were extracted from the results of Gaussian fitting. (**C**) Theoretical transmission spectra for *ac*-HBC and *zc*-HBC junctions. The *p*-HOMOs and *p*-LUMOs are marked using downward and upward triangles, respectively. (**F**) Scattering states of the *p*-HOMOs of *ac*-HBC and *zc*-HBC junctions. The charge transport channels are highlighted using orange dashed boxes, and the charge transport directions are indicated by yellow arrows.

ac-HBC molecule appears at ~9.8×10^{-6} G_0 (≈0.78 nS), which is 5.5 times higher than that of the *zc*-HBC molecule.

These molecular conductance performances indicate that the charge transport through the armchair channel is more efficient than that through the zigzag channel, which is well verified and explained by further quantum transport calculations on the two single-molecule junctions. Figure 2C shows the calculated transmission spectra for *ac*-HBC and *zc*-HBC junctions. The perturbed highest occupied molecular orbitals (*p*-HOMOs) and perturbed lowest unoccupied molecular orbitals (*p*-LUMOs) are marked using downward and upward triangles, respectively. The *zc*-HBC molecule exhibits a smaller HOMO-LUMO bandgap than the *ac*-HBC molecule; this is similar to the characteristics of other carbon-based materials (*21*, *22*). The *p*-HOMOs for the *ac*-HBC and *zc*-HBC molecules are both close to the electrode Fermi level, which means that *p*-HOMO dominates charge transport under certain bias voltages. However, with regard to the transmission coefficients around the Fermi level, that of the *ac*-HBC junction is greater than that of the *zc*-HBC junction, which leads to the *ac*-HBC junction's higher conductance. These results are in good accordance with the above experimental measurements that the charge transport efficiency of the armchair channel is higher than that of the zigzag channel. Moreover, the scattering states of *p*-HOMOs for Au-(*ac*-HBC)-Au and Au-(*zc*-HBC)-Au junctions were simulated and plotted in Fig. 2F. Distinctly, the charge migrating through the armchair channel maintains a higher transmission probability across the entire molecular skeleton than charges passing through the zigzag channel. This result confirms the higher transport efficiency of the armchair channel. Further orbital-decomposed density of state analyses demonstrated that the overlapping p_z orbitals of C atoms along the armchair direction dominated the directional transmission characteristics. As a result, the charge pairs with opposite phases (marked with blue and red in Fig. 1B) are distributed along the armchair channel as the favorable transport direction. Meanwhile, for the Au-(*zc*-HBC)-Au junction, its zigzag channel deviates from the favorable charge transport direction (Fig. 1D), leading to smaller conductance. The zigzag channel can be taken as two parallel armchair channels, between which the charge migrates through quantum tunneling, thus exhibiting a smaller transport efficiency. In addition, we have researched simpler aromatic structures such as poly-*p*-phenylene and anthracene, and theoretical calculations show that poly-*p*-phenylene (anthracene) maintains the same transport characteristics as *ac*-HBC (*zc*-HBC) (figs. S18 and S19).

Charge transport in armchair and zigzag single-molecule devices

To enable further study of the charge transport characteristics through the armchair and zigzag channels, stable graphene-(*ac*-HBC)-graphene [Gr-(*ac*-HBC)-Gr] and Gr-(*zc*-HBC)-Gr single-molecule devices (Fig. 3A) were constructed using a static GMG-SMJ technique (figs. S20 and S21). Specifically, the amino groups on both sides of the HBC molecules are covalently bonded to graphene electrodes with terminal carboxyl groups to form single-molecule junctions with high stability (*23*). The drain current-voltage (I_D-V_D) characteristic curves were then measured, as shown in Fig. 3 (B and C) (figs. S22 and S23). Under a bias voltage of 0.5 V, the average current of the *ac*-HBC device is ~81.9 nA, which is 15 times higher than the ~5.6 nA current of the *zc*-HBC device. The conductance differs by an order of magnitude, which is consistent with the results of the STM-BJ measurements. Correspondingly, the theoretically calculated transmission spectra (Fig. 3D) show that when compared with the transmission spectrum of the *zc*-HBC device, the spectrum of the *ac*-HBC device shows a larger transmission coefficient near the Fermi level, which matches the experimental data well. The scattering states of the Gr-(*ac*-HBC)-Gr and Gr-(*zc*-HBC)-Gr devices were also simulated theoretically (Fig. 3E). Similarly, the charge transport efficiency through the armchair conduction channel is higher than the corresponding efficiency through the zigzag channel.

To explore the intrinsic transport mechanism further, plots of $\ln(I/V^2)$ versus $1/V$ characteristics are analyzed using the Fowler-Nordheim tunneling model (Fig. 3F and figs. S24 and S25). The results show that the inflection point (V_{trans}) for the *ac*-HBC device is ~0.44 V, while that for the *zc*-HBC device is ~0.25 V. According to the Landauer formula and theoretical predictions, these inflection points correspond to a certain proportion of the conductive resonance peak tail entering the bias window (*3*, *24*, *25*). Correspondingly, the theoretically simulated transmission spectra (Fig. 3D) show that the *p*-HOMOs of the *ac*-HBC and *zc*-HBC devices are close to the Fermi level, which means that *p*-HOMO is the dominant charge transport channel. The *p*-HOMO energy level of *zc*-HBC is closer to the Fermi level than that of *ac*-HBC. Therefore, under the same bias voltage, the *p*-HOMO of the *zc*-HBC device enters the bias window first, thus leading to its smaller transition voltage. These different energy band structures and transmission coefficients for the armchair and zigzag channels lay the foundation for specific design of the device functionality.

Field-effect properties of armchair and zigzag channels

Unlike traditional field-effect transistors, single-molecule field-effect transistors (Fig. 4A) use the gate electric field to adjust the positions of their molecular energy levels (fig. S26), thus regulating the conductance of single molecules (*26*–*32*). When compared with that of the armchair channel, the smaller HOMO-LUMO bandgap of the zigzag channel is beneficial in improving the gate regulation efficiency. Furthermore, the lower charge transfer efficiency of the zigzag channel is expected to reduce the device's off-state current, thereby improving the on-off ratio of the device (*33*). To verify these assumptions, the gate modulation processes of the *ac*-HBC and *zc*-HBC single-molecule devices were simulated through theoretical calculations. Figure 4 (B and C) shows that, when the gate voltage V_G changes from −2 to 2 V, the transmission peaks of the *ac*-HBC and *zc*-HBC devices both move sequentially to the left along the energy level. When V_G is in the range between −2 and 0 V, the *p*-HOMO is the dominant charge transport channel because it is closer to the Fermi level. Then, as the gate voltage continues to increase from 0 to 2 V, the *p*-LUMO becomes closer to the Fermi level and the dominant conduction level of the molecule transitions from the *p*-HOMO to the *p*-LUMO. This implies that ambipolar charge transport characteristics should be shown in both *ac*-HBC and *zc*-HBC single-molecule field-effect transistors (*26*). Furthermore, the *p*-HOMO and the *p*-LUMO of *zc*-HBC are both closer to the Fermi level during the gating process (Fig. 4C), which means that the corresponding device exhibits better gate regulation efficiency.

In the experiments, an ionic liquid gate was used to perform single-molecule field effect regulation (fig. S27). Specifically, the *N*,*N*-diethyl-*N*-(2-methoxyethyl)-*N*-methylammonium

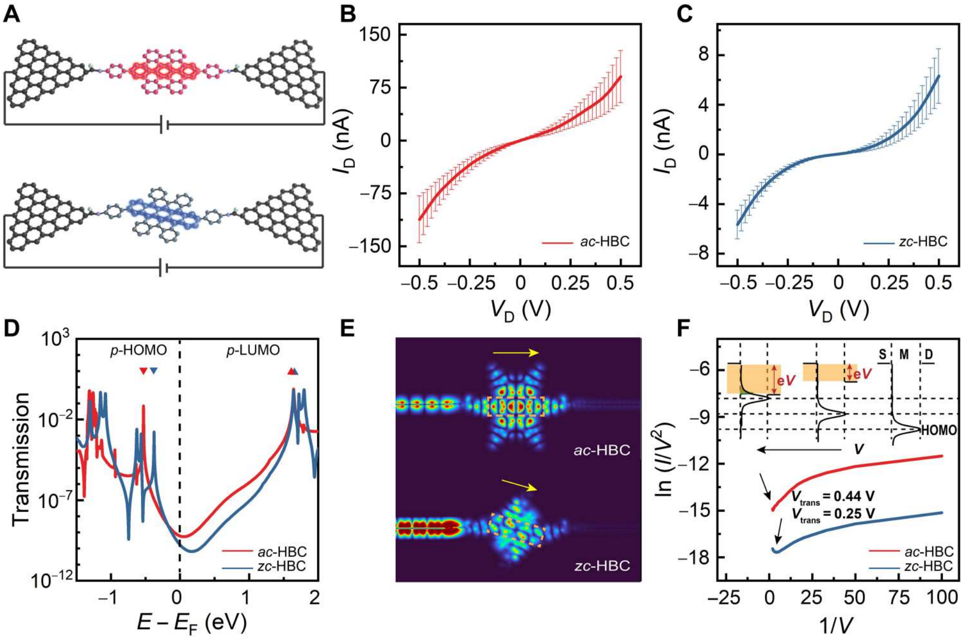

Fig. 3. Charge transport in stable single-molecule devices. (**A**) Schematics of a Gr-(*ac*-HBC)-Gr single-molecule device (top) and a Gr-(*zc*-HBC)-Gr single-molecule device (bottom). (**B** and **C**) I_D versus V_D characteristics with error bars for *ac*-HBC and *zc*-HBC devices (mean of $n = 5$ technical replicates from five different single-molecule devices; error bars indicate SD), respectively. (**D**) Theoretical transmission spectra for the *ac*-HBC and *zc*-HBC devices. The *p*-HOMOs and *p*-LUMOs are marked using downward and upward triangles, respectively. (**E**) Scattering states for the *p*-HOMOs of the *ac*-HBC and *zc*-HBC devices. The charge transport channels and directions are marked using orange dashed boxes and yellow arrows, respectively. (**F**) $\ln(I/V^2)$ versus $1/V$ characteristics for the *ac*-HBC and *zc*-HBC devices. Inset: The Fowler-Nordheim tunneling model is used to provide a qualitative explanation of the inflection point of the curve.

bis(trifluoromethyl sulphonyl)imide (DEME-TFSI) ionic liquid (fig. S28), which has similarly sized anions and cations, high stability, and a wide chemical redox window, was selected. When the gate voltage is applied, an electric double layer with a thickness of ~0.75 nm will form to generate a strong gate electrostatic field up to ~10 MV/cm, thus effectively modulating the molecular energy levels (*26*). In addition, the *ac*-HBC and *zc*-HBC molecules both have moderate HOMO-LUMO energy gaps (Fig. 3D), which help to control their molecular conductive channels through gating.

Typical gate-dependent $|I_D|$-V_D characteristic curves for the Gr-(*ac*-HBC)-Gr and Gr-(*zc*-HBC)-Gr devices are shown in Fig. 4 (D and G), respectively. When V_G varied from −2 to 2 V, $|I_D|$ initially decreased and then increased, thus demonstrating the efficient gate modulation of the single-molecule devices. By monitoring the changes in I_D with V_G at a fixed V_D, the transfer characteristic curves of each device can be obtained to enable further evaluation of the field-effect performance. The device transfer characteristics over the range from $V_D = 0.1$ to 0.5 V (Fig. 4, E and H) show ambipolar charge transport characteristics. The maximal on-off ratio of the *zc*-HBC device is ~185, which is three times that of the *ac*-HBC device with a value of ~62 and is consistent with the theoretical prediction. In addition, fig. S29 shows that, in the presence of both the electric field and the ionic liquid, with or without molecular connections, the leakage current is negligible. To enable further understanding of the field-effect mechanism, 2D visualizations of dI/dV plotted versus both V_G and V_D for the *ac*-HBC and *zc*-HBC devices are shown in Fig. 4 (F and I), respectively. The blue and green low-conductance regions illustrate the off-resonant transport through the HOMO-LUMO gap, and the orange and red high-conductance regions indicate that the conductive frontier molecular orbitals enter the bias window through resonant transport. For both *ac*-HBC and *zc*-HBC devices, the low conductance regions show complete diamond shapes that indicate that the *p*-HOMO or *p*-LUMO for charge transport can enter the bias window at specific gate voltages. This demonstrates the ambipolar charge transport characteristics and shows that the molecular conductance can be adjusted effectively via gating, which is consistent with the predictions from the theoretical simulations.

In this work, HBC molecules with different central structures were designed specifically to create armchair and zigzag channels. Dynamic Au-(*ac*/*zc*-HBC)-Au single-molecule junctions and stable Gr-(*ac*/*zc*-HBC)-Gr single-molecule devices were fabricated to study the armchair and zigzag charge transport properties at the single-molecule and single-channel levels. Both experimental and theoretical studies consistently showed that the armchair channel conductance is approximately one order of magnitude higher than that of the zigzag channel, which indicates that the armchair channel has higher charge transfer efficiency. For field-effect applications, the lower charge transfer efficiency of the zigzag channel means that the *zc*-HBC device has a lower off-state current, thus giving the device a larger on-off ratio. In addition, the molecule with the zigzag channel has a smaller HOMO-LUMO energy bandgap, which also helps to improve the device's field-effect regulation under application of a gate electric field. These studies of armchair and zigzag charge transport provide different perspectives for in-depth understanding of the unique structure-property relationships of these molecules, illustrating the potential of carbon nanomaterials with polycyclic aromatic hydrocarbons for use in a

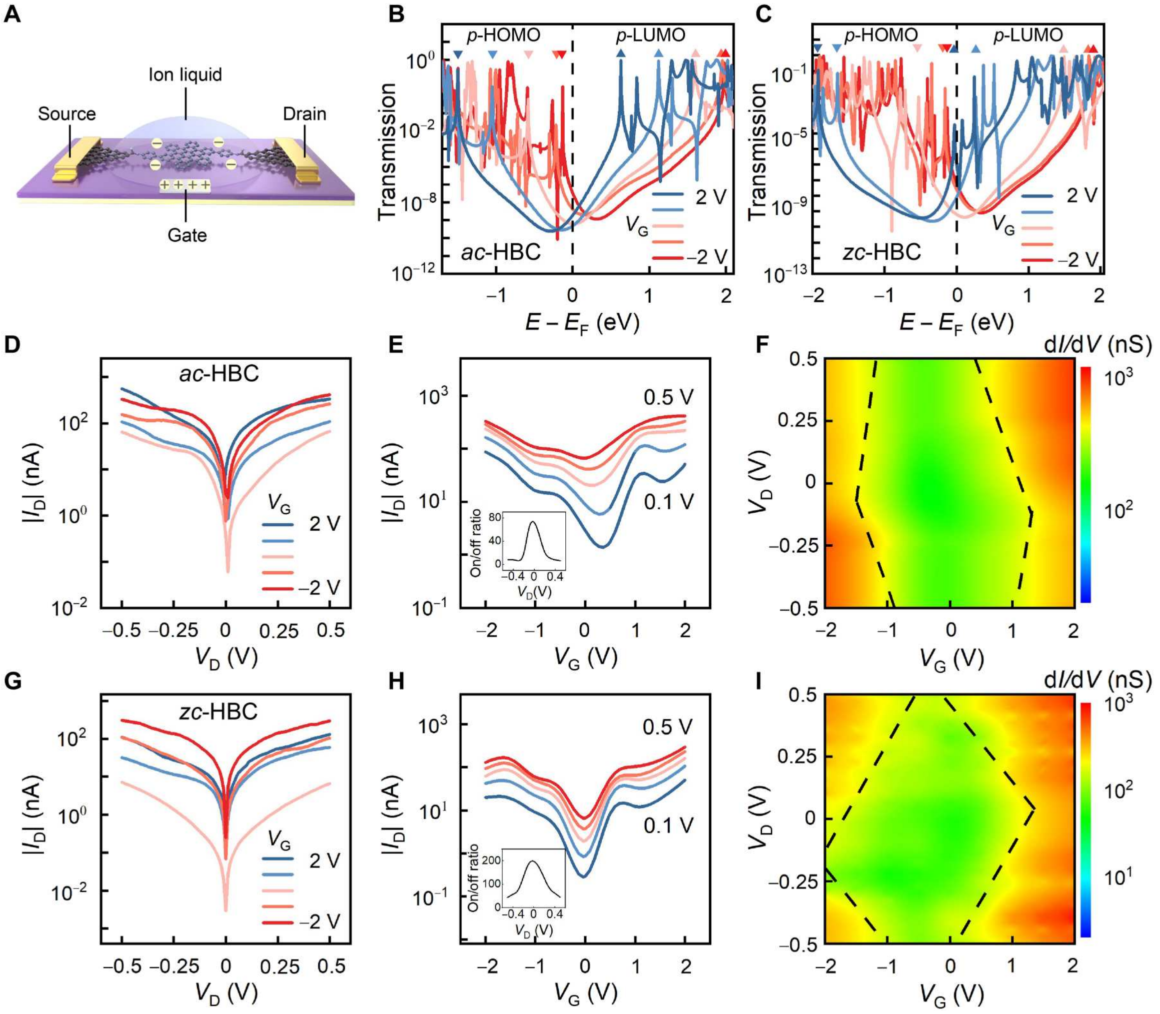

Fig. 4. Field-effect properties of the single-molecule devices. (**A**) Schematic illustration of the single-molecule device structure with ionic liquid gating. (**B** and **C**) Gate-dependent zero-bias transmission spectroscopy characteristics for *ac*-HBC– and *zc*-HBC–based single-molecule devices, respectively, measured over the range from -2 V $\leq V_G \leq 2$ V with steps of 1 V. The *p*-HOMO and *p*-LUMO are indicated by downward and upward triangles, respectively. (**D** and **G**) $|I_D|$ versus V_D characteristics of *ac*-HBC and *zc*-HBC over the range from -2 V $\leq V_G \leq 2$ V with steps of 1 V. (**E** and **H**) Transfer characteristics for *ac*-HBC and *zc*-HBC over the range from $V_D = 0.1$ to 0.5 V with steps of 0.1 V. The insets show the V_D-dependent on/off ratios. (**F** and **I**) 2D visualizations of d*I*/d*V* plotted versus V_G and V_D for *ac*-HBC and *zc*-HBC, respectively. Black dashed lines represent auxiliary markers of the conductance diamond edges.

wide variety of electronic and optoelectronic device applications. At the same time, it also provides the possibility of using carbon nanomaterials to realize device functionalizations.

MATERIALS AND METHODS

Molecular synthesis

See section S1 for detailed information.

Device fabrication and molecular connection

Scanning tunneling microscope break junction

Gold wire (99.99%, 0.25-mm diameter) was purchased from ZhongNuo Advanced Material (Beijing) Technology Co. Ltd. to fabricate the STM-BJ tip. The gold tip was formed by electrochemical etching. Substrates were prepared by depositing a 10-nm–thick chromium film and a 200-nm-thick gold film on a silicon wafer. The target molecules were dissolved in the TCB solvent to perform further measurements.

Graphene-molecule-graphene single-molecule junction

High-quality monolayer graphene was grown on Cu foil by chemical vapor deposition, the graphene was then transferred to SiO_2/Si substrates via wet transfer and patterned into ribbons by photolithography, and the external metal electrodes were fabricated on the graphene sheets by photolithography and thermal evaporation (fig. S20). Nanogap graphene electrodes (fig. S21) with carboxylic acid end groups were fabricated by dotted line lithography, as reported previously (*34*). The amino groups on both sides of the single HBC molecules are linked to the carboxyl groups at the end of the graphene electrodes through a dehydration condensation reaction. The specific operation involves dissolving HBC molecules with a concentration of approximately 10^{-4} M in 10 ml of anhydrous pyridine. Then, graphene devices with nanogaps and 1-ethyl-3-(3-dimethylaminopropyl) carbodiimide hydrochloride (a dehydrating agent/carboxyl activator) were added to the solution. An anhydrous oxygen-free argon atmosphere was maintained to enable the connection between the molecules and the electrodes. After standing for 2 days, the devices were extracted from the solution, washed with appropriate amounts of ultrapure water and acetone to remove any residues, and finally dried with nitrogen.

Device measurements

Scanning tunneling microscope break junction

The distance between the gold tip and the substrate was controlled using a stepper motor and a piezoelectric stack. A bias voltage was applied between the tip and the substrate, and the current was used as the feedback signal to control the movement of the gold tip. During the repeated opening (tip retracting) and closing (tip approaching) cycles, the conductance versus displacement traces were collected, and the traces from the opening cycles were used to perform further analyses. All measurements were taken at room temperature. The single-molecule conductance measurements were performed using the Xtech STM-BJ developed by W. Hong's group at Xiamen University, and the data were analyzed using the XMe open-source code (https://github.com/Pilab-XMU/XMe_DataAnalysis).

Graphene-molecule-graphene single-molecule junction

The electrical properties of the devices were tested using the Keysight B1500A semiconductor characterization system in combination with the Karl Suss PM5 probe station (for the atmospheric environment) and the Lakeshore TTPX probe station (for the vacuum environment) at room temperature. For the current-voltage (I-V) measurements, the sweep interval for V_D was 0.01 V per step. The DEME-TFSI ionic liquid was dropped onto the center of each graphene-based single-molecule device using a microsampler.

Theoretical calculations

Density functional theory (DFT) was adopted to perform the geometric optimization for both the molecules and the two-probe systems (figs. S30 and S31), which mimic the experimental molecular junctions. DFT calculations were carried out using the generalized gradient approximation (GGA) for the exchange-correlation potential, the projector augmented wave method (*35*, *36*), and a plane-wave basis set, as implemented in the Vienna ab initio simulation package (*37*). The energy cutoff for the plane-wave basis was set to 500 eV for all calculations, and vacuum spaces of at least 20 Å in thicknesses between periodic images were used. All atoms in the supercell were allowed to relax until the residual force per atom was lower than 0.01 $\mathrm{eV{\cdot}Å^{-1}}$ for both the molecules and the two-probe systems. For the calculation of HOMO and LUMO energy levels for *ac*(*zc*)-HBC molecules, we adopted the B3LYP/6–311+G (d, p) methodology implemented in the Gaussian 09 package (*38*). The transport properties were calculated within the framework of DFT combined with the nonequilibrium Green's function (NEGF) (*38*) method within the Nanodcal package (*39*–*41*). Succinctly, the NEGF-DFT calculates the density matrix by NEGF as $\rho \sim \int dEG^{<}$, and transmission coefficient as $T = T\gamma[G^{\gamma}\,\Gamma_L\,G^{a}\,\Gamma_R]$, where $G^{<,\gamma,a}$ are the lesser, retarded, and advanced Green's functions, respectively, and $\Gamma_{L,R}$ are the self-energies of the left (L) and right (R) leads. Furthermore, the conductance is $G = T \times e^2/h$, where e is the electron charge and h is the Planck constant. In addition, the norm-conserving pseudopotential was used to describe the core electrons, and the double-ζ polarization linear combination of atomic orbitals was used to describe the valence electrons. The exchange correlation was treated using the GGA_PBE96 functional. In the simulations, the z-direction was set as the transport direction and the y-direction is vertical to the molecule plane. A k-mesh of $1 \times 50 \times 1$ and $12 \times 50 \times 1$ was used in the calculations of Au lead and graphene lead, respectively, and a k-mesh of $1 \times 1 \times 1$ and $12 \times 1 \times 1$ was used in the calculations of the Au-probed and graphene-probed devices, respectively.

Supplementary Materials

This PDF file includes:
Sections S1 to S5
Figs. S1 to S31
References

REFERENCES AND NOTES

1. D. V. Kosynkin, A. L. Higginbotham, A. Sinitskii, J. R. Lomeda, A. Dimiev, B. K. Price, J. M. Tour, Longitudinal unzipping of carbon nanotubes to form graphene nanoribbons. *Nature* **458**, 872–876 (2009).
2. O. V. Yazyev, A guide to the design of electronic properties of graphene nanoribbons. *Acc. Chem. Res.* **46**, 2319–2328 (2013).
3. C. Jia, J. Wang, C. Yao, Y. Cao, Y. Zhong, Z. Liu, Z. Liu, X. Guo, Conductance switching and mechanisms in single-molecule junctions. *Angew. Chem. Int. Ed.* **52**, 8666–8670 (2013).
4. Y. Zang, S. Ray, E.-D. Fung, A. Borges, M. H. Garner, M. L. Steigerwald, G. C. Solomon, S. Patil, L. Venkataraman, Resonant transport in single diketopyrrolopyrrole junctions. *J. Am. Chem. Soc.* **140**, 13167–13170 (2018).
5. P. Li, Y. Chen, B. Wang, M. Li, D. Xiang, C. Jia, X. Guo, Single-molecule optoelectronic devices: Physical mechanism and beyond. *Opto Electron Adv.* **5**, 210094 (2022).
6. Y. Li, M. Buerkle, G. Li, A. Rostamian, H. Wang, Z. Wang, D. R. Bowler, T. Miyazaki, L. Xiang, Y. Asai, G. Zhou, N. Tao, Gate controlling of quantum interference and direct observation of anti-resonances in single molecule charge transport. *Nat. Mater.* **18**, 357–363 (2019).
7. J. Liu, X. Huang, F. Wang, W. Hong, Quantum interference effects in charge transport through single-molecule junctions: Detection, manipulation, and application. *Acc. Chem. Res.* **52**, 151–160 (2019).
8. C. Tang, L. Huang, S. Sangtarash, M. Noori, H. Sadeghi, H. Xia, W. Hong, Reversible switching between destructive and constructive quantum interference using atomically precise chemical gating of single-molecule junctions. *J. Am. Chem. Soc.* **143**, 9385–9392 (2021).
9. S. Li, H. Yu, K. Schwieter, K. Chen, B. Li, Y. Liu, J. S. Moore, C. M. Schroeder, Charge transport and quantum interference effects in oxazole-terminated conjugated oligomers. *J. Am. Chem. Soc.* **141**, 16079–16084 (2019).
10. Z. Li, M. Smeu, A. Rives, V. Maraval, R. Chauvin, M. A. Ratner, E. Borguet, Towards graphyne molecular electronics. *Nat. Commun.* **6**, 6321 (2015).
11. P. Shen, M. Huang, J. Qian, J. Li, S. Ding, X.-S. Zhou, B. Xu, Z. Zhao, B. Z. Tang, Achieving efficient multichannel conductance in through-space conjugated single-molecule parallel circuits. *Angew. Chem. Int. Ed.* **59**, 4581–4588 (2020).
12. G. Povie, Y. Segawa, T. Nishihara, Y. Miyauchi, K. Itami, Synthesis of a carbon nanobelt. *Science* **356**, 172–175 (2017).
13. Y. Yano, N. Mitoma, K. Matsushima, F. Wang, K. Matsui, A. Takakura, Y. Miyauchi, H. Ito, K. Itami, Living annulative π-extension polymerization for graphene nanoribbon synthesis. *Nature* **571**, 387–392 (2019).
14. D. Lu, G. Zhuang, H. Wu, S. Wang, S. Yang, P. Du, A large π-extended carbon nanoring based on nanographene units: Bottom-up synthesis, photophysical properties, and selective complexation with fullerene C_{70}. *Angew. Chem. Int. Ed.* **56**, 158–162 (2017).
15. M. Ball, Y. Zhong, Y. Wu, C. Schenck, F. Ng, M. Steigerwald, S. Xiao, C. Nuckolls, Contorted polycyclic aromatics. *Acc. Chem. Res.* **48**, 267–276 (2015).
16. S. Xiao, S. J. Kang, Y. Zhong, S. Zhang, A. M. Scott, A. Moscatelli, N. J. Turro, M. L. Steigerwald, H. Li, C. Nuckolls, Controlled doping in thin-film transistors of large contorted aromatic compounds. *Angew. Chem. Int. Ed.* **52**, 4558–4562 (2013).
17. S. Xiao, M. Myers, Q. Miao, S. Sanaur, K. Pang, M. L. Steigerwald, C. Nuckolls, Molecular wires from contorted aromatic compounds. *Angew. Chem. Int. Ed.* **44**, 7390–7394 (2005).

18. O. G. Ziogos, S. Konstantinopoulos, L. Tsetseris, D. N. Theodorou, Computational studies of nanographene systems: Extended discotics, covalently linked "supermolecules," and functionalized supramolecular assemblies. *J. Phys. Chem. C* **122**, 18715–18731 (2018).
19. W. Pisula, X. Feng, K. Müllen, Charge-carrier transporting graphene-type molecules. *Chem. Mater.* **23**, 554–567 (2011).
20. J. Wu, W. Pisula, K. Müllen, Graphenes as potential material for electronics. *Chem. Rev.* **107**, 718–747 (2007).
21. Z. Shi, R. Yang, L. Zhang, Y. Wang, D. Liu, D. Shi, E. Wang, G. Zhang, Patterning graphene with zigzag edges by self-aligned anisotropic etching. *Adv. Mater.* **23**, 3061–3065 (2011).
22. Y.-W. Son, M. L. Cohen, S. G. Louie, Energy gaps in graphene nanoribbons. *Phys. Rev. Lett.* **97**, 216803 (2006).
23. C. Jia, A. Migliore, N. Xin, S. Huang, J. Wang, Q. Yang, S. Wang, H. Chen, D. Wang, B. Feng, Z. Liu, G. Zhang, D. Qu, H. Tian, M. Ratner, H. Xu, A. Nitzan, X. Guo, Covalently bonded single-molecule junctions with stable and reversible photoswitched conductivity. *Science* **352**, 1443–1445 (2016).
24. Y. Kim, K. Im, H. Song, Charge transport characteristics of molecular electronic junctions studied by transition voltage spectroscopy. *Materials* **15**, 774 (2022).
25. C. Jia, X. Guo, Molecule–electrode interfaces in molecular electronic devices. *Chem. Soc. Rev.* **42**, 5642–5660 (2013).
26. N. Xin, X. Li, C. Jia, Y. Gong, M. Li, S. Wang, G. Zhang, J. Yang, X. Guo, Tuning charge transport in aromatic-ring single-molecule junctions via ionic-liquid gating. *Angew. Chem. Int. Ed.* **57**, 14026–14031 (2018).
27. W. Y. Lo, W. Bi, L. Li, I. H. Jung, L. Yu, Edge-on gating effect in molecular wires. *Nano Lett.* **15**, 958–962 (2015).
28. Xu, Xiao, X. Yang, L. Zang, Tao, Large gate modulation in the current of a room temperature single molecule transistor. *J. Am. Chem. Soc.* **127**, 2386–2387 (2005).
29. N. Xin, C. Hu, H. Al Sabea, M. Zhang, C. Zhou, L. Meng, C. Jia, Y. Gong, Y. Li, G. Ke, X. He, P. Selvanathan, L. Norel, M. A. Ratner, Z. Liu, S. Xiao, S. Rigaut, H. Guo, X. Guo, Tunable symmetry-breaking-induced dual functions in stable and photoswitched single-molecule junctions. *J. Am. Chem. Soc.* **143**, 20811–20817 (2021).
30. J. Li, S. Pudar, H. Yu, S. Li, J. S. Moore, J. Rodríguez-López, N. E. Jackson, C. M. Schroeder, Reversible switching of molecular conductance in viologens is controlled by the electrochemical environment. *J. Phys. Chem. C* **125**, 21862–21872 (2021).
31. H. Fu, C. Zhao, J. Cheng, S. Zhou, P. Peng, J. Hao, Z. Liu, X. Gao, C. Jia, X. Guo, Dipole-improved gating of azulene-based single-molecule transistors. *J. Mater. Chem. C* **10**, 7803–7809 (2022).
32. Z. Yan, X. Li, Y. Li, C. Jia, N. Xin, P. Li, L. Meng, M. Zhang, L. Chen, J. Yang, R. Wang, X. Guo, Single-molecule field effect and conductance switching driven by electric field and proton transfer. *Sci. Adv.* **8**, eabm3541 (2022).
33. L. Meng, N. Xin, C. Hu, H. Al Sabea, M. Zhang, H. Jiang, Y. Ji, C. Jia, Z. Yan, Q. Zhang, L. Gu, X. He, P. Selvanathan, L. Norel, S. Rigaut, H. Guo, S. Meng, X. Guo, Dual-gated single-molecule field-effect transistors beyond Moore's law. *Nat. Commun.* **13**, 1410 (2022).
34. Y. Cao, S. Dong, S. Liu, L. He, L. Gan, X. Yu, M. L. Steigerwald, X. Wu, Z. Liu, X. Guo, Building high-throughput molecular junctions using indented graphene point contacts. *Angew. Chem. Int. Ed.* **51**, 12228–12232 (2012).
35. G. Kresse, D. Joubert, From ultrasoft pseudopotentials to the projector augmented-wave method. *Phys. Rev. B* **59**, 1758–1775 (1999).
36. P. E. Blöchl, Projector augmented-wave method. *Phys. Rev. B* **50**, 17953–17979 (1994).
37. H. J. Monkhorst, J. D. Pack, Special points for brillouin-zone integrations. *Phys. Rev. B* **13**, 5188–5192 (1976).
38. A.-P. Jauho, N. S. Wingreen, Y. Meir, Time-dependent transport in interacting and noninteracting resonant-tunneling systems. *Phys. Rev. B* **50**, 5528–5544 (1994).
39. J. Taylor, H. Guo, J. Wang, Ab initio modeling of quantum transport properties of molecular electronic devices. *Phys. Rev. B* **63**, 245407 (2001).
40. J. Taylor, H. Guo, J. Wang, Ab initio modeling of open systems: Charge transfer, electron conduction, and molecular switching of a C_{60} device. *Phys. Rev. B* **63**, 121104 (2001).
41. J. Maassen, M. Harb, V. Michaud-Rioux, Y. Zhu, H. Guo, Quantum transport modeling from first principles. *Proc. IEEE* **101**, 518–530 (2013).
42. R. Yamaguchi, S. Hiroto, H. Shinokubo, Synthesis of oxygen-substituted hexa-peri-hexabenzocoronenes through Ir-catalyzed direct borylation. *Org. Lett.* **14**, 2472–2475 (2012).
43. M. Brandbyge, J. L. Mozos, P. Ordejón, J. Taylor, K. Stokbro, Density-functional method for nonequilibrium electron transport. *Phys. Rev. B.* **65**, 165401 (2002).

Acknowledgments

Funding: We acknowledge primary financial support from the National Key R&D Program of China (2021YFA1200102, 2021YFA1200101, and 2022YFE0128700), the National Natural Science Foundation of China (22173050, 22150013, 12104313, 2225108, 21772123, 21727806, and 21933001), the Tencent Foundation through the XPLORER PRIZE, the Fundamental Research Funds for the Central Universities (63223056), "Frontiers Science Center for New Organic Matter" at Nankai University (63181206), the Natural Science Foundation of Beijing (2222009), Beijing National Laboratory for Molecular Sciences (BNLMS202105), Shanghai Engineering Research Center of Green Energy Chemical Engineering (18DZ2254200), "111" Innovation and Talent Recruitment Base on Photochemical and Energy Materials (D18020), Shanghai Government (21010503400 and 18JC1412900), and International Joint Laboratory of Resource Chemistry (IJLRC). We also acknowledge HZWTECH for providing computation facilities. **Author contributions:** X.G., C.J., S.X., X.K., and P.D. conceived and designed the experiments. M.Z. and P.L. fabricated the devices. M.Z., H.J., and Y.L. did the molecular synthesis. M.Z., P.L., J.H., L.M., and Z.Y. performed the device measurements. Z.W. performed the theoretical calculations. X.G., C.J., S.X., X.K., P.D., J.W., E.Z., and M.Z. analyzed the data and wrote the paper. All the authors discussed the results and commented on the manuscript. **Competing interests:** The authors declare that they have no competing interests. **Data and materials availability:** All data needed to evaluate the conclusions in the paper are present in the paper and/or the Supplementary Materials.

Submitted 23 December 2022
Accepted 27 April 2023
Published 31 May 2023
10.1126/sciadv.adg4346

Science Advances

Distinct armchair and zigzag charge transport through single polycyclic aromatics

Miao Zhang, Zewen Wu, Hongxing Jia, Peihui Li, Lei Yang, Jie Hao, Jinying Wang, Enyu Zhang, Linan Meng, Zhuang Yan,
Yi Liu, Pingwu Du, Xianghua Kong, Shengxiong Xiao, Chuancheng Jia, and Xuefeng Guo

Sci. Adv., **9** (22), eadg4346.
DOI: 10.1126/sciadv.adg4346

Science Advances (ISSN) is published by the American Association for the Advancement of Science. 1200 New York Avenue NW, Washington, DC 20005. The title *Science Advances* is a registered trademark of AAAS.